ACS OMEGA

Open Access

http://pubs.acs.org/journal/acsodf

Article

Single-Step Synthesis of Laser-Induced Graphene (LIG) Wood Impregnated SnO_2−NiO for Room Temperature Methane Gas Sensor

Hafiza Sana Haider, Meiling Pan, Wei Jin, Xiangting Zhang, Yanqing Ma,* and Lei Ma*

Cite This: *ACS Omega* 2026, 11, 24334−24345

Read Online

ACCESS | Metrics & More | Article Recommendations | Supporting Information

ABSTRACT: The development of low-power, environmentally friendly gas sensors is critical for next-generation safety and environmental monitoring, yet it is constrained by energy-intensive operation and unsustainable fabrication processes. We present a one-step laser-induced method to fabricate a wood-based resistive methane sensor, where laser irradiation directly converts a natural wood precursor into a 3D conductive laser-induced graphene (LIG) network decorated with in situ-formed SnO_2−NiO heterojunction nanoparticles. This integrated SnO_2−NiO/LIG nanocomposite features a hierarchical, porous, polycrystalline structure, as characterized by SEM, TEM, Raman, XRD, and XPS. The sensor operates at ambient temperature, has a response time of 50 s, achieves a low theoretical detection limit of 7 ppm, and maintains robust performance under varying humidity of ≤70%. The sensing superiority is attributed to synergistic effects at the n-SnO_2/p-NiO heterointerface within the conductive graphene matrix, which facilitates efficient charge separation and transfer upon gas exposure, validated by density functional theory (DFT) calculations. This direct laser-engraving, solvent free approach using wood establishes a new paradigm for designing sustainable, cost-effective, and eco-friendly, high-performance nanoarchitecture gas sensors.

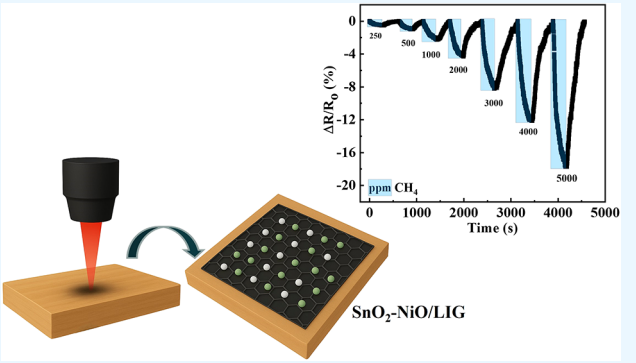

1. INTRODUCTION

Methane (CH_4) is a potent greenhouse gas with a global warming potential 25 times greater than carbon dioxide (CO_2) over a 100-year time frame, and it contributes significantly to climate change.[1,2] Beyond its environmental impact, CH_4 poses severe explosion risk in confined spaces (e.g., coal mines, oil/gas facilities, and biogas plants) where concentrations of 5−15% by volume can lead to catastrophic accidents.[3] Consequently, reliable CH_4 detection is crucial for industrial safety, environmental monitoring, and occupational health.[4] However, detecting trace amounts of CH_4 remains challenging owing to its nonpolar molecular structure and high C−H bond dissociation energy (439 kJ/mol), which limit its interaction with sensing materials.[5]

Current CH_4 detection technologies, including laser-spectroscopic hollow optical sensors, and electrochemical sensors, offer high accuracy but suffer from critical drawbacks such as high power consumption (>1 W), slow response/recovery times (min to hours), limited stability, and portability.[6,7] These constraints are particularly problematic for applications in wearable electronics and sensor networks, where energy efficiency and miniaturization are crucial for personalized health and real-time environmental monitoring.[8] Solid-state gas sensors based on metal oxide semiconductors (MOS), such as tin oxide (SnO_2), nickel oxide (NiO), and zinc oxide (ZnO), provide a low-cost and scalable alternative.[9,10] However, conventional MOS gas sensors require elevated operating temperatures (140−300 °C) to activate surface redox reaction, leading to excessive energy consumption, long-term drift, and poor stability for real-time detection.[10,11]

To address these limitations, carbon-based hybrid nanomaterials, such as graphene and reduced graphene oxide (rGO), have been explored for their high surface area and excellent charge-carrier mobility, which leverage synergistic effects to enhance sensitivity for CH_4 gas.[12,13] The formation of a p−n junction and defect mediated gas adsorption mechanism can enhance sensor response. For example, the nanocomposite SnO_2/rGO[14] or SnO_2@rGO1%[15] exhibits a response of 47.6% to 1000 ppm methane at 150 °C with a response/recovery time of 61 s/5 min, and SnO_2 decorated NiO[16] porous nanosheets sensor demonstrates excellent CH_4 sensing performance, exhibiting a high response at an optimal temperature of 330 °C. The combination of the large specific surface area and high conductivity of carbon nanomaterials facilitates the adsorption of gas molecules, thereby increasing

Received: December 29, 2025
Revised: March 27, 2026
Accepted: April 8, 2026
Published: April 15, 2026

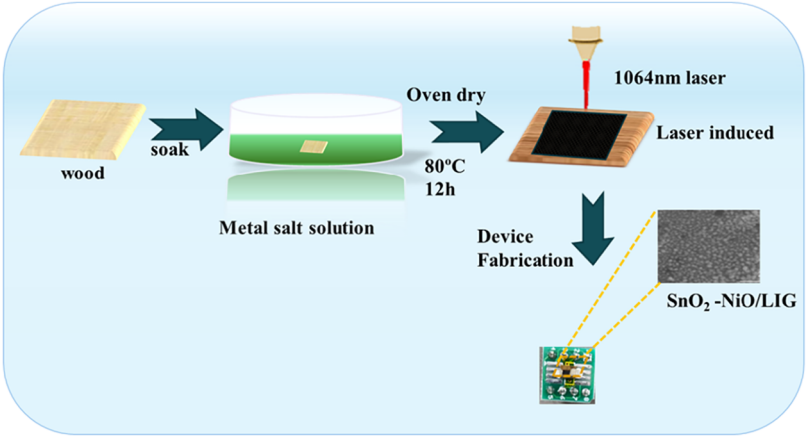

Figure 1. Schematic setup for SnO_2−NiO/LIG fabrication on the wood surface.

conductivity.[17] Despite these improvements, two critical challenges remain unresolved: (1) Fundamental reliance on high operating temperature, which limit energy efficiency, (2) Expensive graphene fabrication methods, such as CVD, epitaxial, or rGO produced via chemical methods, which involve toxic reagents and generate hazardous chemical waste, raising environmental sustainability and scalability concerns.[18]

In 2014, Tour et al. first reported the fabrication of high-quality patterned graphene by laser induction on polyimide (PI) films, offering a rapid, solvent-free, and scalable alternative to rGO.[19] This technique enables the synthesis of porous 3D graphene via laser irradiation of carbon-rich precursors (e.g., polyimide, polymers). The resulting multilayer formation has emerged as a crucial design principle for optimizing charge-transfer pathways, thereby improving overall sensing performance.[20,21] However, the nonbiodegradable nature of synthetic substrates like PI and PET undermines environmental sustainability. This results in poor adhesion, mechanical failures, and increased electronic waste.[22] To overcome this limitation, researchers have successfully explored lignin-rich biomass, particularly wood, as an alternative precursor offering high surface area, tunable conductivity, and porous structure that provides abundant active sites.[23−26] While laser-induced graphene (LIG) exhibits promising sensing performance for NO_2[27] and NH_3,[28] its inherent sensitivity to nonpolar, inert gases such as CH_4 is limited. Dosi et al. partially addressed this by functionalizing LIG with Pd nanoparticles for electrochemical CH_4 sensors.[29] Despite significant progress, a critical research gap persists: (1) there is no demonstrated strategy that simultaneously achieves a one-step, low-cost fabrication avoiding complex energy-intensive procedures without toxic chemicals or noble metals, (2) Sustainable, high surface area natural substrate, and (3) High sensitivity at room temperature to nonpolar CH_4 molecules. Recent advances in chemiresistive sensing suggest that 3D-SnO_2 nanostructures offer high surface area and a wide band gap, for gas absorption and desorption,[30] while the integration of catalytic p-type NiO creates heterojunctions and heterointerface engineering by creating an internal electric field that promotes electron−hole separation to facilitate charge transfer and selective gas detection.[31,32] Even though SnO_2−NiO heterojunctions have been studied to enhance gas sensing through modulation of depletion layers and Schottky barriers, their integration with 3D conductive scaffolds like wood-derived LIG for room-temperature CH_4 sensing via chemiresistive mechanisms has not been reported previously.

This work aims to bridge this gap by developing a room-temperature CH_4 sensor based on a one-step synthesis of wood-derived LIG substrate impregnated with a SnO_2−NiO heterojunction. The synergistic interaction between the porous 3D conductive network and the optimized SnO_2−NiO interface enhances CH_4 adsorption and charge transfer without external heating. First-principles DFT calculations confirm enhanced CH_4 adsorption energy at the heterojunction interface and the associated enhancement of charge transfer, providing a fundamental understanding of the sensitivity improvement. Through systematic optimization, the sensor achieves a low detection limit of 7 ppm, high selectivity against interfering gases, and excellent long-term stability, demonstrating a one-step, sustainable, low-cost, and practical strategy for ambient methane detection.

2. EXPERIMENTAL SECTION

2.1. Materials

Nickel nitrate, hexahydrate (Ni $(NO_3)_2{\cdot}6H_2O$, 98%) and Tin chloride, dihydrate ($SnCl_2{\cdot}2H_2O$, 98%) were provided by Beijing InnoChem Science & Technology Co, Ltd., and Tianjin Heowns Biochemical Technology Co, Ltd., respectively. A CH_4 gas cylinder was purchased from Tianjin Boliming Technology Co., Ltd.

2.2. Characterization

The surface morphology of the samples was characterized by scanning electron microscopy (SEM, Hitachi, SU-3500) and Transmission electron microscopy (JEOL JEM-200). Energy-dispersive X-ray spectroscopy (EDS, IXRF system, SU-3500) was used to characterize the elements and their distributions. The Raman spectra were obtained using a Raman spectrometer (ANDOR-MARZHAUSER) with a 532 nm laser. The X-ray photoelectron spectroscopy (XPS, Thermo Scientific) was used to analyze surficial constituents. The binding energies were extracted from the calibrated C 1s line at 284.6 eV. X-ray diffraction (XRD, Dandong Tongda Technology, TD-3500) was used to analyze the crystallinity and lattice constants of the composite.

2.3. Fabrication of Gas Sensors

As shown in Figure 1, MO NPs/LIG (metal oxide nanoparticles/laser-induced graphene) were fabricated using a one-step laser induction process under ambient conditions. Basswood was cut into $3 \times 3 \times 1.5$ mm^3 thin slices, cleaned in ultrapure water for 30 min, and soaked in a solution mixture of 1.5 g of nickel nitrate hexahydrate and 2.25 g of tin chloride dihydrate in 10 mL of deionized water for 24 h. Then take it out, rinse it with deionized water to wash off excess

https://doi.org/10.1021/acsomega.5c13608
ACS Omega 2026, 11, 24334−24345

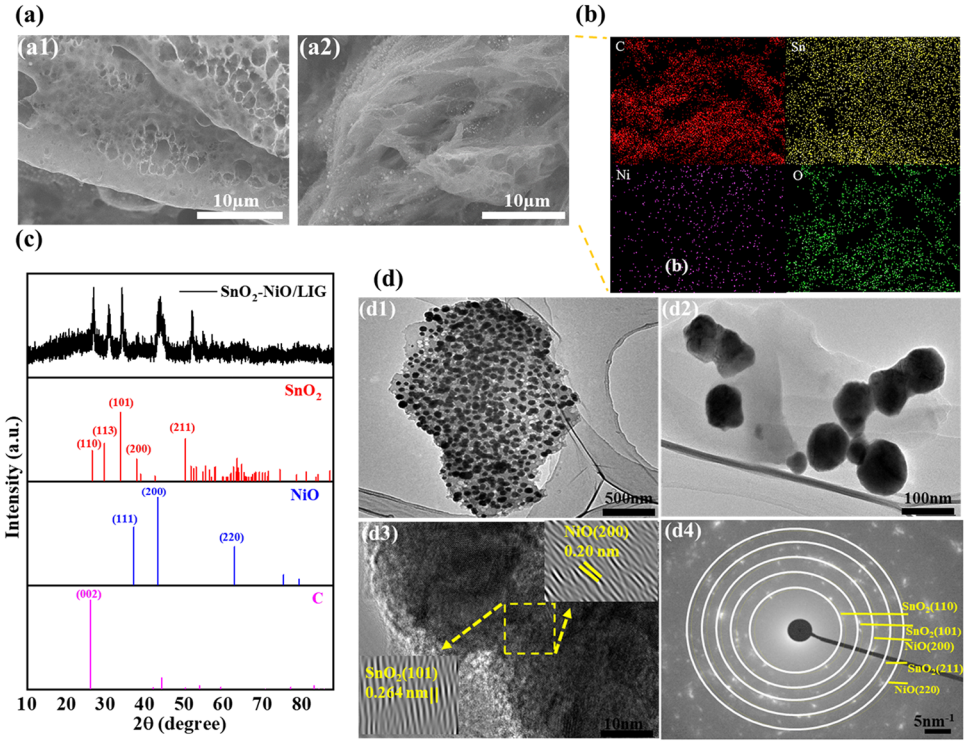

Figure 2. (a) SEM image of Wood-based metal oxide laser-induced graphene composite, (a1) SnO_2/LIG; (a2) SnO_2−NiO/LIG, (b) energy dispersive spectroscopy (EDS) mapping (C), (Sn), (Ni), and (O), (c) XRD pattern of SnO_2−NiO/LIG, and (d) (d1−d4) TEM, HRTEM and SAED pattern of SnO_2−NiO/LIG composite.

metal salts, and dry it in an oven at 80 °C for 12 h. The basswood slices were scribed with a 1064 nm CO_2 laser over a 1 × 2 mm area to convert lignocellulose to graphene and oxidized metal ions to metal oxides. As a natural material, basswood is a good candidate for hybridization with other inorganic structures and for conversion to graphene due to its high lignocellulose content.[33] The laser parameters were then adjusted to optimize the structure for a uniform distribution of SnO_2−NiO nanoparticles and improved graphene quality. The laser scanning speed was set to 1500 mm/s, and 5 laser scans were performed with varying powers (0.09 W, 0.15 W, 0.24 W, 0.30 W and 0.45 W, respectively). The synthesized composite was attached to a printed circuit board (PCB) using polyimide tape, and conductive silver paste was applied to both sides to make the final CH_4 gas sensor device.

2.4. Testing of Gas Sensors

The prepared sensor was placed in a custom-built gas-sensing measurement system, as schematically illustrated in Figure S1. To quantify its performance, we define responsivity (R_e) as in eq 1.

$$R_e = \frac{R_o - R_g}{R_o} \times 100\% \quad (1)$$

where R_g is the resistance corresponding to the maximum resistance change after exposure to the target gas, and R_o is the initial resistance. Response Time (R_T) can be defined as the time required for the resistance of the sensor to reach 60% of its change after exposure to the target gas. The theoretical limit of detection (LOD) is calculated using the equation.[30]

$$\mathrm{LOD} = \frac{3 \times \mathrm{RMS}_{\mathrm{noise}}}{\mathrm{Sensitivity}} \quad (2)$$

where RMS_{noise} refers to the root-mean-square of baseline noise levels measured before CH_4 exposure and RMS_{noise} was calculated using the baseline Figure S5 and eq S1 in the Supporting Information.

2.5. Theoretical Metrics

Theoretical simulations were conducted using the Vienna Ab initio Simulation Package (VASP 5.4.1). The projector-augmented wave method was employed to describe the ion-electron interactions with a cutoff energy of 450 eV. The generalized gradient approximation (GGA) with the PBE exchange-correlation functional was used to treat the electronic exchange correlation interactions. A vacuum layer of 15 Å was set up to avoid interactions between periodic structures. The Brillouin zones were sampled with 2 × 2 × 1 and 4 × 4 × 1 Monkhorst−Pack meshes for geometry optimization and electronic structure calculations, respectively. Convergence criteria were defined as 10^{-6} eV for electronic self-consistent loops and 0.02 eV/Å for ionic relaxation. The DFT + U correction was considered for the calculations in this study. The chosen values of the Hubbard correction U were 10, 5, 5, 5 eV for C, Ni, Sn, and O, respectively. The dispersion corrections in Grimme's scheme (DFT-D3) scheme were applied to describe van der Waals interactions. The charge transfer analysis was performed by the Hirshfeld charge group method.

3. RESULTS AND DISCUSSION

3.1. Device Structure and Characterization

Figure 2(a1-a2) illustrates the SEM image of SnO_2/LIG and SnO_2−NiO/LIG composites synthesized by laser irradiation from the basswood substrate pretreated with metal salt solution. After laser irradiation, a three-dimensional porous carbon skeleton with a high abundance of uniformly dispersed nanoparticles forms on the surface. The elemental mapping analysis shown in Figure 2b confirms that C, Sn, Ni, and O are uniformly distributed within the detected region, corroborating the SEM findings and indicating the homogeneous incorporation of Sn and Ni nanoparticles into the graphene structure. In Figure 2c, the diffraction peaks from XRD analysis at 26.85, 29.74, 33.35, 38.84, and 51.63° correspond to (110), (113),

https://doi.org/10.1021/acsomega.5c13608
ACS Omega 2026, 11, 24334−24345

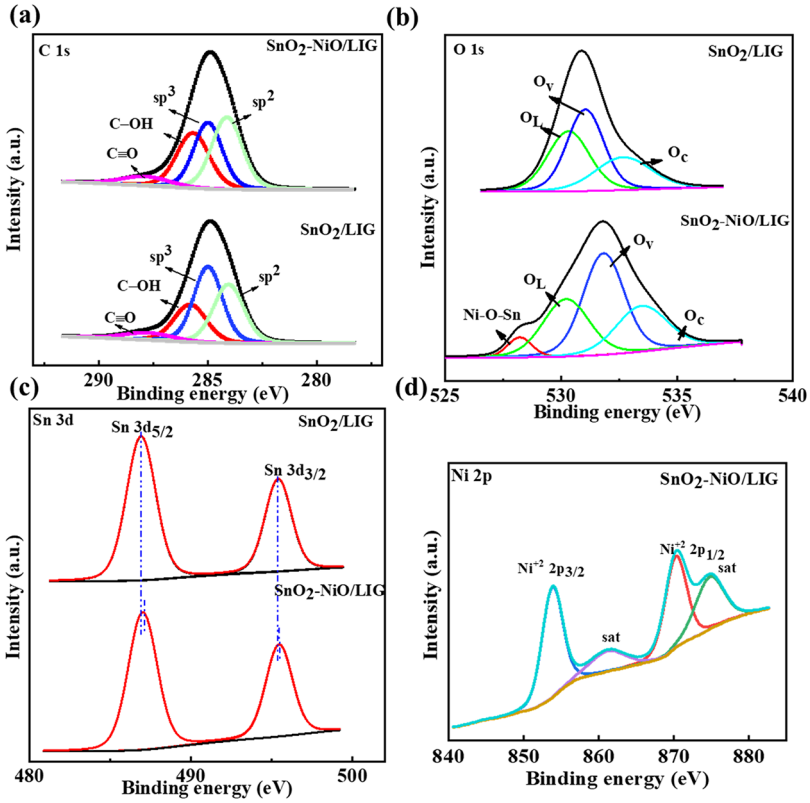

Figure 3. XPS spectra of wood-based SnO_2/LIG, SnO_2−NiO/LIG composites (a) C 1s, (b) O 1s, (c) Sn 3d, and (d) Ni 2p spectra of SnO_2−NiO/LIG.

(101), (200), and (211) of SnO_2 nanoparticles.[34] The emissions of all the reflection planes were attributed to the tetragonal rutile structure. The diffraction peaks at 37.24, 43.27, and 62.86°, corresponding to the (111), (200), and (220) crystal planes, can be indexed to nickel oxide nanoparticles (JCPDS 71-1179). In addition, the diffraction peak at 26.8° corresponds to (002) of graphite (JCPDS 75-16210).

Figure 2d presents the comprehensive microstructural characterization of the synthesized SnO_2−NiO/LIG nanocomposite. The low and high-magnification TEM images in Figure 2d(d1,d2) reveal the successful formation of well-dispersed spherical NiO and SnO_2 nanoparticles uniformly anchored on the LIG substrate. The HRTEM image in Figure 2d(d3) shows distinct lattice fringes with interplanar spacings of 0.264 and 0.20 nm, corresponding to the (101) plane of rutile SnO_2 and the (200) plane of cubic NiO, respectively. The crystallinity and phase composition are further confirmed by the SAED pattern in Figure 2d(d4). The concentric diffraction rings are indexed to the (110), (101), and (211) planes of SnO_2, along with the (200) and (220) planes of NiO. These observations are consistent with the XRD results of JCPDS No. 41-1445 and JCPDS No. 71-1179. The presence of these distinct rings confirms the polycrystalline nature of the composite material. Notably, the established heterointerface network among NiO, SnO_2, and graphene is expected to enhance charge carrier transfer kinetics by generating abundant active sites and interfacial electric fields.

To analyze the surface chemical state of SnO_2/LIG and SnO_2−NiO/LIG composite in detail, X-ray photoelectron spectroscopy (XPS) measurements were conducted. The fine spectra of C, O, Sn, and Ni elements are shown in Figure 3. C 1s in Figure 3a C 1s consists of four peaks, with binding energies of 284.04, 284.98, 285.84, and 287.84 eV, respectively, corresponding to C=C sp^2 bond, C−C sp^3 bond, C−OH bond, and C=O bond.[35,36] The prominent peak at 284.04 eV indicates a high degree of graphitization in the carbon framework, which aligns with Raman spectroscopy results. The peak at 284.98 eV indicates structural defects or amorphous carbon regions, corresponding to the porous carbon structure observed by SEM. Peaks at 285.84 and 287.84 eV are attributed to oxygen-containing functional groups (C−OH and C=O), arising from residual oxidation groups formed during the laser-induction process. Figure 3b shows the O 1s spectra of the two samples with SnO_2/LIG and SnO_2−NiO/LIG. Both the O 1s spectra are fitted into three peaks. The binding energies at about 530.3, 531.05, and 532.75 eV of pure SnO_2/LIG and SnO_2−NiO/LIG with binding energies at 528.22 eV for Ni−O−Sn,[37] 530.3, 531.8, and 533.5 eV corresponds to the lattice oxygen(O_L), oxygen vacancies (O_v), and chemisorbed oxygen species (O_c) or OH species, respectively. In contrast, the peaks at 531.8 and 533.5 eV of SnO_2−NiO/LIG exhibit a little chemical shift in binding energies as compared to SnO_2/LIG. Notably, the O_v and O_c levels in SnO_2−NiO/LIG are higher than in pure SnO_2/LIG, likely due to lattice oxygen transfer from the interaction between NiO and SnO_2. These surface oxygen vacancies (O_v) and lattice oxygen (O_c) are crucial for gas adsorption, providing more active sites for electron transfer during redox reactions, which enhance the gas-sensing performance.[16,38] Subsequently, the Sn 3d high-resolution XPS spectra of SnO_2/LIG and SnO_2−NiO/LIG are carried out as shown in Figure 3c, which exhibits two characteristic peaks corresponding to Sn $3d_{5/2}$ and Sn $3d_{3/2}$ orbitals at 486.8 and 495.5 eV with a

https://doi.org/10.1021/acsomega.5c13608
ACS Omega 2026, 11, 24334−24345

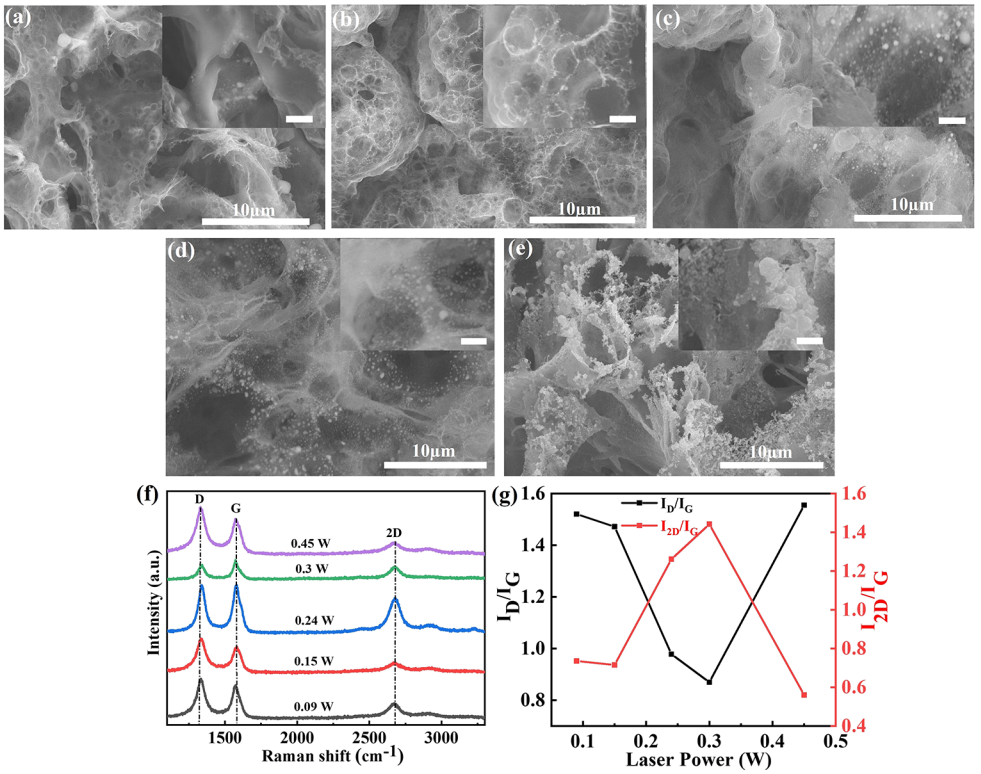

Figure 4. SEM images of wood-based SnO_2−NiO/LIG composites prepared by laser power of (a) 0.09 W, (b) 0.15 W, (c) 0.24 W, (d) 0.30 W, and (e) 0.45 W, with insets showing higher magnification images (scale bar = 2 μm) using 1064 nm laser wavelength at 1500 mm/s scanning speed and 5 number of laser scans. (f) Raman spectra of wood-based SnO_2−NiO/LIG composites prepared at 1064 nm wavelength under different laser powers, and (g) I_D/I_G and I_{2D}/I_G ratio.

binding energy difference of 0.2 eV.[31] These results confirm a change in the oxidation state of Sn from Sn^{2+} to Sn^{4+} during laser irradiation. The Ni 2p spectrum shown in Figure 3d exhibits four primary peaks at 853.85 eV (Ni^{2+} $2p_{3/2}$), 870.32 eV (Ni^{2+} $2p_{1/2}$), 861.35 eV, and 874.79 eV, showing the presence of Ni(II) satellite peaks, suggesting Ni primarily exists in the composite as NiO.[39] These characterization results conclusively confirm the successful synthesis of a SnO_2−NiO/LIG heterojunction composite via a facile, one-step laser-induced method using a metal salt-impregnated wood substrate.

The laser processing structure relationship of the SnO_2−NiO/LIG is systematically investigated by varying key laser processing parameters, such as laser power at a constant scanning speed of 1500 mm/s and 5 laser scans. Laser power significantly influences the morphology of the wood-derived SnO_2−NiO/LIG nanocomposites, as shown by SEM analysis in Figure 4. At the lowest power of 0.09 W, Figure 4a, the photon energy is too weak for complete carbonization, resulting in irregular, shallow pores and a loosely connected carbonaceous structure. This under-processed matrix lacks anchoring sites, resulting in a sparse, uneven distribution of SnO_2−NiO nanoparticles. The sensor has a limited active surface area and poor gas accessibility, resulting in a small CH_4 response. Increasing the power to 0.15 W, in Figure 4b, improved irradiation, creating a better-developed porous, foam-like network with more uniform, though moderate, nanoparticle coverage. This increased the number of active sites for gas adsorption, and the response to CH_4 also increased. Optimal morphology appears at intermediate powers of 0.24 and 0.3 W, as shown in Figure 4c,d. Here, the energy input was sufficient for efficient pyrolysis, converting wood into a well-defined, three-dimensional honeycomb-like porous network of graphene. This structure provides a high density of uniform anchoring sites, promoting a dense and even dispersion of SnO_2−NiO nanoparticles. This ideal balance of high porosity for rapid gas diffusion, electrical conductivity, and maximum active surface area from both the LIG and the well-dispersed nanoparticles correlates directly with the improved CH_4 sensing performance observed at these power levels. Conversely, at an excessive power of 0.45 W in Figure 4e, localized overheating degrades the LIG framework. The porous network collapses, and the SnO_2−NiO nanoparticles get agglomerated,[40] greatly reducing the active surface area and weakening the structural integrity necessary for gas adsorption. This morphological degradation explains the subsequent decline in sensor performance at high laser powers. In summary, the carbonaceous morphology evolves from incomplete porous sheets with sparse, nonuniform distribution of SnO_2−NiO nanoparticles at low laser power, to an optimal honeycomb network with uniform, well-dispersed nanoparticles at intermediate power, before deteriorating into compact, collapsed structures with agglomerated NPs at excessive power. This morphological progression directly dictates the CH_4 sensing properties, with intermediate powers favoring the ideal structure for high-performance detection.[41]

The vibrational and structural characteristics of wood-based SnO_2−NiO/LIG composites were evaluated via Raman spectroscopy. As shown in Figure 4f, the spectra exhibit three characteristic peaks of graphitic carbon: the D-band (1342.70 cm^{-1}) associated with structural defects, the G-band (1572.77 cm^{-1}) representing the E_{2g} phonon mode of sp^2-

https://doi.org/10.1021/acsomega.5c13608
ACS Omega 2026, 11, 24334−24345

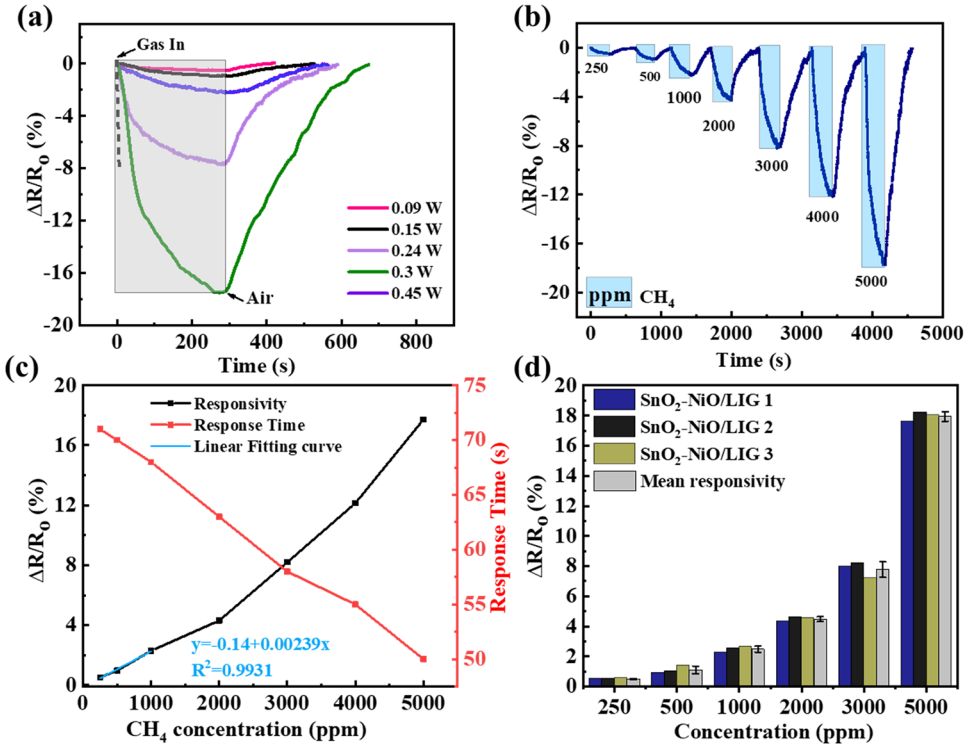

Figure 5. Performance characterization of the SnO_2−NiO/LIG-based gas sensor, (a) response curve of SnO_2−NiO/LIG samples prepared at different laser power to 0.5% of methane, (b) dynamic response curve to methane from 250 to 5000 ppm at room temperature, (c) the corresponding calibration curve with a linear fitting for responsivity and response time, (d) repeatability test of for multiple SnO_2−NiO/LIG samples.

hybridized carbon, and the 2D-band (2676.76 cm^{-1}) which is the second-order overtone of the D-band indicative of the successful formation of a 3D porous graphene structure.[42,43] A quantitative analysis of peak intensity ratios (I_D/I_G) reveals a strong dependence of the microstructural quality on the incident laser power. As shown in Figure 4g low power range (0.09 to 0.3W), the I_D/I_G value decreased notably from 1.5 to 0.8, indicating a reduction in lattice defects and an increase in graphitization. This trend explains that the photothermal energy provided was sufficient to facilitate defect healing and the formation of distinct, high-quality graphene layers. At the 0.3W threshold, the material achieves an optimal balance, characterized by a stabilized low I_D/I_G ratio (0.85) and a relatively high I_{2D}/I_G ratio (1.48), confirming the preservation of high crystallinity and a layered graphene framework. Increasing the power to 0.45 W results in a sharp increase in the I_D/I_G ratio (1.55), reflecting substantial structural disorder. Simultaneously, the I_{2D}/I_G ratio decreases significantly, indicating a loss of graphene crystallinity, likely due to photothermal ablation from excessive laser energy. Eventually, the laser power of 0.3 W is identified as the optimal processing parameter. It balances the formation of a porous graphene structure with controlled defects and a uniform dispersion of SnO_2−NiO nanoparticles. This optimized microstructure provides a high-conductivity backbone and abundant active sites, serving as the foundation for the enhanced gas-sensing performance observed in this study.[44]

3.2. Gas Sensing Measurements

The following gas-sensing tests were carried out at room temperature (23 °C), and 40% relative humidity unless otherwise specified. The experimental setup used for testing is shown in Figure S1. The gas sensor based on SnO_2−NiO/LIG exhibits a larger and yet more stable response than those based on SnO_2/LIG in Figure S2, due to the heterojunction formation. It is observed that all gas sensors exhibit increased responsivity upon exposure to 5000 ppm of CH_4 (0−300 s), and subsequently recover to their baseline when switched back to air (after 300 s). Varying the SnO_2−NiO concentration further yields an optimized concentration value that enhances the response to methane gas, as shown in the SEM images in Figure S3 and in the gas-sensing response test in Figure S4.

The effect of laser irradiation power (0.09−0.45 W) on the methane-sensing capabilities of SnO_2−NiO/LIG nanocomposite was evaluated to determine the optimal response. As shown in Figure 5a, the sensor fabricated at 0.3 W exhibits the highest responsivity of 18% for 0.5% of CH_4 among all samples. This superior performance is intrinsically linked to the optimized microstructural evolution of the sensing layer. SEM analysis in Figure 4d shows that the 0.3 W SnO_2−NiO/LIG sample exhibits a very uniform distribution of SnO_2 and NiO nanoparticles throughout the 3D porous graphene framework. Furthermore, Raman spectra in Figure 4f confirm that the sample prepared at this power produces high-quality graphene with an I_{2D}/I_G ratio of 1.48, and a defect-enriched structure (I_D/I_G = 0.85), providing the necessary active sites for gas−solid interactions.

Figure 5b shows the SnO_2−NiO/LIG sensor's response to CH_4 from 250 to 5000 ppm, with the blue shaded region indicating exposure to the target gas. The response rises quickly, peaks around 5 min, then gradually recovers after the gas flow is stopped. Response amplitude was calculated with eq 1. To quantitatively evaluate the sensor's responsivity and response time at different concentrations, the relevant

https://doi.org/10.1021/acsomega.5c13608
ACS Omega 2026, 11, 24334−24345

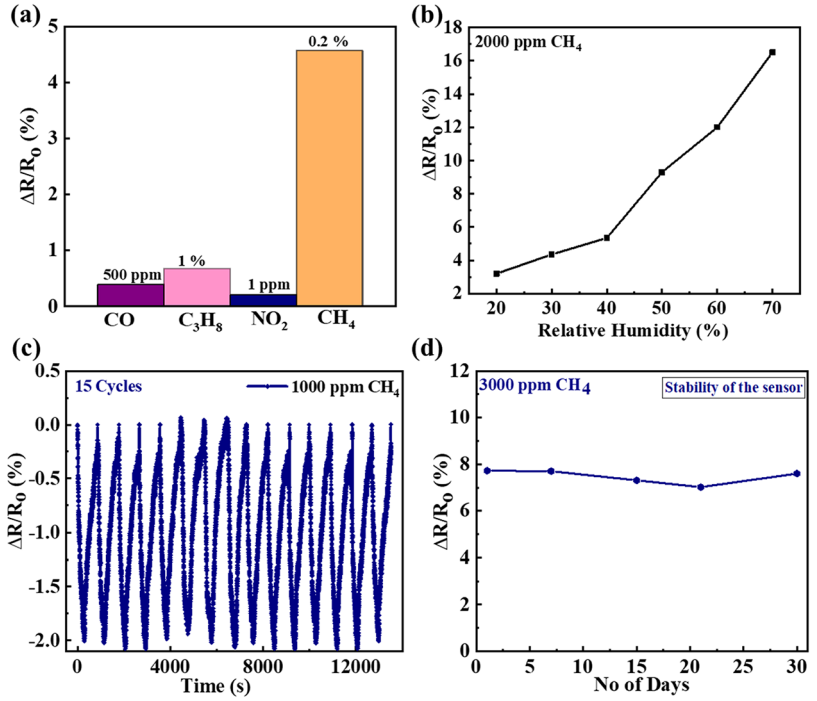

Figure 6. Performance characterization of the SnO_2−NiO/LIG gas sensor, (a) selectivity test of the gas sensor to methane over the other interfering gases, (b) response of the SnO_2−NiO/LIG sensor at different relative humidity, (c) repeatability test of the gas sensor over 15 consecutive cycles, and (d) long-term stability of the gas sensor to 3000 ppm of methane over 30 days.

parameters extracted from Figure 5b are plotted in Figure 5c. The responsivity increases from 0.5 to 18% as the CH_4 concentration rises from 250 to 5000 ppm, indicating that the response to the gas analyte is directly proportional to the gas concentration. The sensor's response decreases because fewer gas molecules at lower concentrations are available to adsorb on the sensor's active surface. As the gas adsorption is concentration-dependent. Therefore, at low concentrations, the adsorption rate was slow, leading to less interaction and a low response. Simultaneously, the response time of the sensor decreases from 71 to 50 s as CH_4 concentration increases, becoming relatively stable above 1000 ppm. The shortened response time at higher concentrations was due to enhanced adsorption dynamics and electron-transfer processes.[45] Additionally, Figure 5c includes a linear fitting for responsivity versus CH_4 concentration at low concentrations (250 ppm-1000 ppm). The obtained calibration curve gave a slope of 0.00239, has a linear regression coefficient (R^2) value of 0.993, leading to the calculated theoretical limit of detection (LOD) of 7 ppm using eq 2 with baseline calculation as shown in Figure S5. The LOD was significantly lower than the threshold limit of (5%) for CH_4,[46] thus enabling precise trace-level detection and early warning capability. To ensure the scientific reliability of these results, the repeatability of the fabrication process was verified using three independent SnO_2−NiO/LIG samples prepared with identical parameters. As shown in Figure 5d the sensors exhibit remarkable consistency. The low standard deviation across the replicates, represented by a mean responsivity of 17.94 ± 0.32% at 5000 ppm, confirms that the one-step laser induction method is highly reproducible and the resulting p-n heterojunction provides stable electronic modulation for gas sensing.

The cross-sensitivity of the SnO_2−NiO/LIG sensor was evaluated against various interfering gases Figure 6a. The SnO_2−NiO/LIG gas sensor exhibits a response of 4.57% to 2000 ppm of CH_4, demonstrating good selectivity against interfering gases. For comparison, the sensor shows only minimal responses of 0.39% to 500 ppm of CO, 0.20% to 1 ppm of NO_2, and 0.6 to 1% C_3H_8 (different concentrations for these gases reflect varied detection thresholds in practical applications).[47] This pronounced selectivity toward CH_4 is attributed to the optimized electronic properties of the SnO_2−NiO heterojunction. The established interfacial energy levels facilitate efficient charge transfer, specifically with CH_4 molecules, via favorable physisorption interactions at room temperature. To validate the sensor's performance under realistic environmental conditions, we assessed its humidity resistance, cyclic stability, and long-term stability, as shown in Figure 6b−d, respectively. The sensor's response to 2000 ppm of CH_4 under varying humidity levels (20−70% RH) is shown in Figure 6b. The response increases progressively from approximately 3 to 16.5% as relative humidity rises. This enhancement can be attributed to a synergistic effect between water vapor and methane adsorption. At room temperature, physiosorbed H_2O molecules act as electron donors, which lowers the baseline resistance of the p-n heterojunction. Furthermore, a physiosorbed water layer promotes protonic conduction across the porous LIG framework via the Grotthuss mechanism, enhancing charge transfer and amplifying the measured response to CH_4.[48] To maintain good linearity, a humidity sensor could be incorporated to calibrate and improve accuracy under practical operating conditions. Figure 6c shows the sensor's repeatability over 15 consecutive ON-OFF cycles of exposure to 1000 ppm of CH_4 gas. During repeated testing, the response showed excellent cyclic reproducibility with no significant drift. The long-term stability of the sensor was evaluated over a 30-day period, with measurements recorded every 7 days, as shown in Figure 6d.

https://doi.org/10.1021/acsomega.5c13608
ACS Omega 2026, 11, 24334−24345

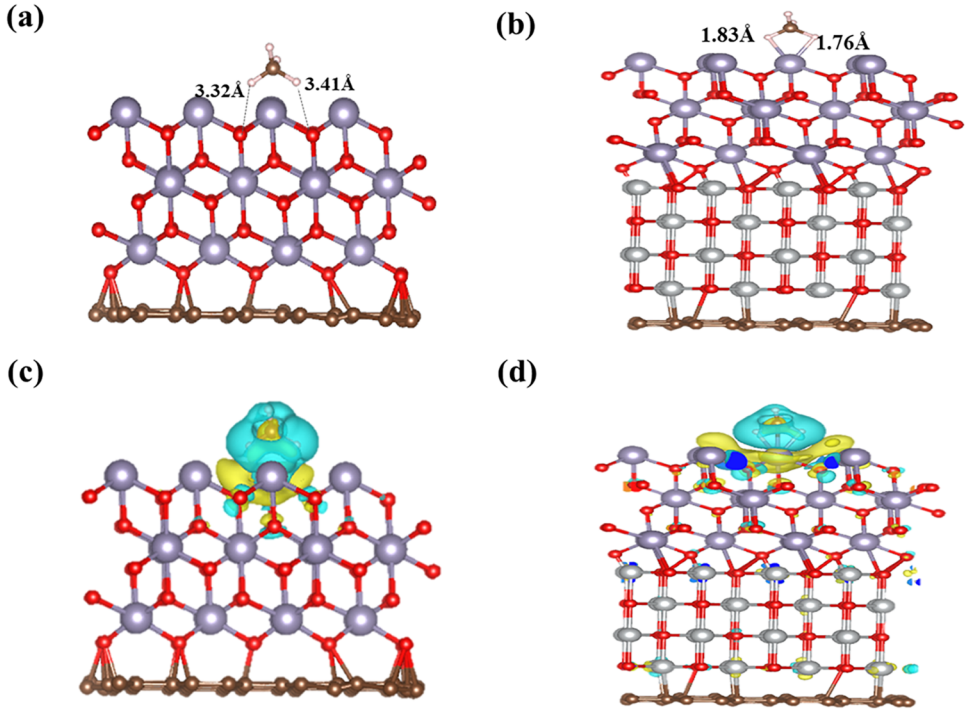

Figure 7. Structural models of CH_4 adsorption on (a) SnO_2 (101)/graphene, and (b) SnO_2 (101)-NiO (200)/graphene surface; charge density difference diagrams of CH_4 adsorption on (c) SnO_2(101)/graphene surface, and (d) SnO_2 (101)-NiO (200)/graphene surface.

The results demonstrate excellent operational stability, with the sensor retaining over 98% of its initial response without significant fluctuation or degradation throughout the testing period. This durability is attributed to the robust chemical and mechanical integration of the SnO_2−NiO heterojunction within the porous, wood-derived LIG matrix. The three-dimensional framework prevents material degradation and ensures consistent electronic transport pathways over extended periods.

3.2.1. DFT+U Analysis. Gas sensing measurements demonstrate that the SnO_2−NiO/LIG sensor exhibits a significantly enhanced response to CH_4 compared to the individual SnO_2/LIG sample, as shown in Figure S2. To elucidate the physical basis for this improvement, critical parameters, including adsorption energy and charge density distribution, were calculated using (DFT+U). Our computational findings suggest that the synergistic interaction between SnO_2 and NiO on the graphene surface is the primary driver for the sensing enhancement.

To determine how SnO_2−NiO/graphene composite enhances the sensor response as compared to SnO_2/graphene, it is possible to calculate the adsorption energy, which allows for the determination of the interaction strength between CH_4 molecules and the SnO_2−NiO decorated graphene surface. A more negative adsorption energy indicates a stronger binding between the molecules and the surface, resulting in a more stable adsorption configuration.[9] DFT+U calculations were performed to study CH_4 adsorption on the SnO_2 (101)/graphene and the SnO_2 (101)-NiO (200)/graphene, as shown in Figure 7a,b. The SnO_2 (101) and NiO (200) crystal planes, which are most prominent in the composite's XRD and TEM results (Figure 2c,d) and the most stable, were selected for this study. The optimized adsorption structures are shown in Figure 7, with the corresponding adsorption energies listed in Table 1. For SnO_2 (101)/graphene, we consider the adsorption of CH_4 at the top of Sn, as well as the hollow position of Sn and the top position of O, and it is found that the adsorption structure of CH_4 binding to the top of Sn is the most stable, with an adsorption energy of −0.641 eV. Notably, the SnO_2−NiO/graphene had the highest adsorption energy of −3.285 eV, much higher than that of the individual components. These findings confirm that the NiO-SnO_2 heterostructure on graphene provides the most energetically favorable environment for CH_4 adsorption, suggesting the potential for faster, more sensitive CH_4 detection. Bader charge analysis was used to further clarify the adsorption mechanism, as shown in Figure 7c,d. The net charge transfers from SnO_2/graphene, and SnO_2−NiO/graphene to CH_4 were calculated as −0.182 and −0.393 electrons, respectively. Therefore, the SnO_2−NiO/graphene heterostructure combines high adsorption energy with significant charge transfer, indicating that the heterointerface plays a vital role in CH_4 gas adsorption and thereby enhances the response.

Table 1. Adsorption Energies of the CH_4 Molecule on SnO_2 (101)/Graphene, and SnO_2 (101)-NiO (200)/Graphene Surfaces

surface model	adsorption energy (eV)	charge transfer (e^-)
SnO_2 (101)/ graphene	−0.641	−0.182
SnO_2 (101)-NiO (200)/ graphene	−3.285	−0.393

3.2.2. Gas Sensing Mechanism. The SnO_2−NiO/LIG composite exhibits exceptional methane sensing properties at room temperature, which can be attributed to three primary factors.

First, the sensing mechanism is rooted in a surface-mediated redox reaction.[49] As illustrated in Figure 8, the interaction between the composite and the surrounding gas occurs in two stages. In ambient air, oxygen molecules adsorb onto the SnO_2

https://doi.org/10.1021/acsomega.5c13608
ACS Omega 2026, 11, 24334−24345

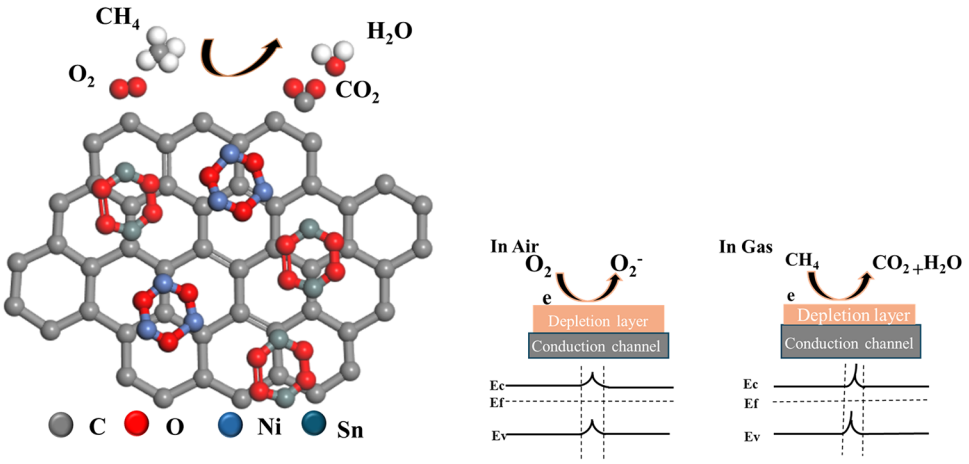

Figure 8. Schematics of the gas sensing mechanism of SnO_2−NiO/LIG CH_4 gas sensor.

Table 2. Comparison of the Developed Sensor's CH_4 Gas Performance with Values Reported in the Literatures

sensing material	techniques	concentration (ppm)	temperature (°C)	response/recovery time	LOD	ref
SnO_2/rGO	hydrothermal	1000−10,000	150	369 s/-	-	12
Pd-SnO_2/rGO	hydrothermal	800−10,000	RT	5 min/7 min	-	49
SnO_2@rGO	hydrothermal	1000−10,000	150	61 s/330 s	-	15
SnO_2(QDs)	precipitation	400−5000	200	1 min/1 min	-	50
SnO_2@rGO-PANI	chemical-polymerization	100−10,000	RT	360 s/1150 s	<100 ppm	51
NiO/ZnO microsphere	hydrothermal	100−1000	RT (UV light)	32 s/180 s	4 ppm	39
NiO/RGO	hydrothermal	100−1000	260	-	-	52
SnO_2/NiO	calcination	500−7000	330	28 s/44 s	-	16
VO_2	hydrothermal	1000−5000	50	35 s/-	-	53
PbS $_{CQD}$	chemical method	5000−70,000	RT	15 s/300 s	-	54
SnO_2-NiO/LIG	laser induction	250−5000	RT	50 s/300 s	7 ppm	this work

and NiO surfaces and are converted into ionosorbed oxygen species (O_2^-) by capturing free electrons from the semiconductor conduction bands.[31] This electron-trapping process is described by eq 3 and 4. The experimental existence of these active sites is confirmed by XPS O 1s analysis Figure 4b, where the prominent peaks corresponding to chemisorbed oxygen (O_c) and oxygen vacancy (O_v) indicate the availability of energy states that facilitate room-temperature gas interaction.

$$O_{2(gas)} \rightarrow O_{2(ads)} \quad (3)$$

$$O_{2(ads)} + e^- \rightarrow O^-_{2(ads)} \quad (4)$$

$$CH_4 + 2O_{2^-} \rightarrow CO_2 + 2H_2O + 2e^- \quad (5)$$

When the sensor is exposed to methane, these oxygen anions react with the target gas molecules, triggering the release of trapped electrons back into the system as shown in eq 5. This injection of electrons reduces the hole concentration in the p-type NiO and narrows the depletion width in the n-type SnO_2, leading to a measurable change in resistance as shown in Figure 8.

Second, the formation of internal SnO_2−NiO/LIG heterostructures is fundamental to the enhanced performance. The contact between SnO_2 and NiO creates a p-n heterojunction that serves as a highly sensitive transducer. Figure S6 shows the current−voltage (I−V) characteristics of the materials. In contrast to the linear, ohmic behavior observed in the individual SnO_2/LIG and NiO/LIG samples, the SnO_2−NiO/LIG composite exhibits clear nonlinear rectification. This confirms the presence of a built-in potential barrier that amplifies the electrical response upon gas adsorption, as reflected in the response and recovery dynamics shown in Figure 5b.

Furthermore, LIG substrate provides a highly conductive, porous 3D framework with a large specific surface area, facilitating rapid gas diffusion and electron transport.[41] Its abundant defect sites further promote charge transfer between SnO_2−NiO nanoparticles and the LIG network, ensuring fast response and recovery at room temperature.

This work shows that our developed SnO_2−NiO/LIG sensor can meet the requirement for fast detection of CH_4 gas at RT, which can greatly reduce power consumption, simplify the process of sensor preparation, and contribute to the development and application of miniaturized, high-end gas sensors as compared to earlier reported work in Table 2. Meanwhile, given its sustainable, simple synthesis routes, SnO_2−NiO/LIG has broad application prospects for CH_4 gas sensors in industries and environmental monitoring.

4. CONCLUSION

In conclusion, this study establishes a sustainable, one-step laser-fabrication strategy for a wood-based SnO_2−NiO/LIG methane sensor, bridging eco-friendly manufacturing with high-performance gas sensing. We engineered an optimized SnO_2−NiO/LIG composite by tuning the laser parameters, resulting in a uniform nanoparticle distribution and a defect-enriched graphene lattice. This SnO_2−NiO/LIG exhibits excellent responsivity supported by both DFT calculations and experimental evidence of robust p-n heterojunction formation. Beyond technical performance, the theoretical

https://doi.org/10.1021/acsomega.5c13608
ACS Omega 2026, 11, 24334−24345

LOD of 7 ppm, 30-day stability, and moisture resilience of (≤70% RH) validate the device's readiness for practical industrial safety monitoring. Future efforts will focus on the scalability of this approach, enabling the fabrication of integrated sensing arrays for simultaneous detection of multiple gases, and on implementing machine-learning-assisted pattern recognition for complex environments, paving the way for the next generation of green and intelligent environmental sensing technologies.

■ ASSOCIATED CONTENT

Supporting Information

The Supporting Information is available free of charge at https://pubs.acs.org/doi/10.1021/acsomega.5c13608.

Gas measurement system, response curves of the gas sensors, SEM images of the gas sensors, time-dependent response curves of the sensor, and $I-V$ test curves (PDF)

■ AUTHOR INFORMATION

Corresponding Authors

Yanqing Ma − *Tianjin International Center for Nanoparticles and Nanosystems, Tianjin University, Tianjin 300072, P. R. China; Tianjin Key Laboratory of Low-dimensional Electronic Materials and Advanced Instrumentation, Tianjin 300072, P. R. China; Haihe Laboratory for Low-dimensional Electronic Materials, Tianjin 300074, P. R. China; School of Precision Instrument and Opto-electronics Engineering, Tianjin University, Tianjin 300072, P. R. China;* orcid.org/0000-0002-3317-8273; Email: mayanqing@tju.edu.cn

Lei Ma − *Tianjin International Center for Nanoparticles and Nanosystems, Tianjin University, Tianjin 300072, P. R. China; Tianjin Key Laboratory of Low-dimensional Electronic Materials and Advanced Instrumentation, Tianjin 300072, P. R. China; Haihe Laboratory for Low-dimensional Electronic Materials, Tianjin 300074, P. R. China;* orcid.org/0000-0002-2446-4833; Email: lei.ma@tju.edu.cn

Authors

Hafiza Sana Haider − *Tianjin International Center for Nanoparticles and Nanosystems, Tianjin University, Tianjin 300072, P. R. China*

Meiling Pan − *Tianjin International Center for Nanoparticles and Nanosystems, Tianjin University, Tianjin 300072, P. R. China*

Wei Jin − *Tianjin International Center for Nanoparticles and Nanosystems, Tianjin University, Tianjin 300072, P. R. China*

Xiangting Zhang − *Tianjin International Center for Nanoparticles and Nanosystems, Tianjin University, Tianjin 300072, P. R. China*

Complete contact information is available at: https://pubs.acs.org/10.1021/acsomega.5c13608

Author Contributions

H.S.H.: Methodology, investigation, data curation, carrying out experiments, writing—original draft preparation. M.P.: Theoretical simulation. W.J.: Investigation, data curation. X.Z.: Investigation, data curation. Y.M.: Writing—review and editing, funding acquisition, supervision. L.M.: Conceptualization, methodology, funding acquisition, supervision, writing—review and editing.

Notes

The authors declare no competing financial interest.

■ ACKNOWLEDGMENTS

This work was financially supported by the National Key R&D Program of China (No. 2022YFC3006303), the Tianjin Natural Science Foundation Project (No. 25JCZDJC01380), and the Innovation Fund of Haihe Laboratory of Low-dimensional Electronic Materials (25HHDWSS00005).

■ REFERENCES

(1) Thakur, S.; Solanki, H. Role of methane in climate change and options for mitigation-a brief review. *Int. Assoc. Biol. Comput. Dig.* **2022**, *1*, 2583−3995.

(2) Folberth, G. A.; Jones, C. D.; O'Connor, F. M.; Gedney, N.; Griffiths, P. T.; Wiltshire, A. J. Drivers of persistent changes in the global methane cycle under aggressive mitigation action. *npj Clim. Atmos. Sci.* **2025**, *8* (1), No. 136, DOI: 10.1038/s41612-024-00867-z.

(3) Mar, K. A.; Unger, C.; Walderdorff, L.; Butler, T. Beyond CO_2 equivalence: The impacts of methane on climate, ecosystems, and health. *Environ. Sci. Policy* **2022**, *134*, 127−136.

(4) Sun, X.; Tang, M.; Yu, M.; Fan, Y.; Qin, C.; Cao, J.; Wang, Y. UV-activated CH_4 gas sensor based on Pd@Ni/ZnO microspheres. *Mater. Today Commun.* **2024**, *40*, No. 109551.

(5) Lam, K. C.; Huang, B.; Shi, S.-Q. Room-temperature methane gas sensing properties based on in situ reduced graphene oxide incorporated with tin dioxide. *J. Mater. Chem. A* **2017**, *5* (22), 11131−11142.

(6) Yang, B.; Xu, J.; Wang, C.; Xiao, J. A potentiometric sensor based on SmMn2O5 sensing electrode for methane detection. *Mater. Chem. Phys.* **2020**, *245*, No. 122679, DOI: 10.1016/j.matchemphys.2020.122679.

(7) Kapit, J. A.; Youngs, S.; Pardis, W. A.; Padilla, A. M.; Michel, A. P. M. An Underwater Methane Sensor Based on Laser Spectroscopy in a Hollow Core Optical Fiber. *ACS Sens.* **2024**, *9* (11), 5896−5905.

(8) Hu, Y.; Hao, P.; Du, B.; Gao, Y.; Yang, W.; Han, M.; Hao, Z.; Duan, H.; Ding, X.; Luo, S. Continuous and freeform manufacturing of hybrid laser-induced graphene and polyimide woven fabrics for enabling smart-textile garments with multifunctional wearable applications. *Chem. Eng. J.* **2025**, *521*, No. 166142.

(9) Hu, X.; Gui, Y.; Zhu, S.; Chen, X. Transition metal oxides (NiO, SnO_2, In_2O_3) modified graphene: A promising candidate to detect and scavenge CO, C_2H_2, and CH_4 gases. *Diamond Relat. Mater.* **2022**, *123*, No. 108856, DOI: 10.1016/j.diamond.2022.108856.

(10) Zhang, B.; Wang, Y.; Meng, X.; Zhang, Z.; Mu, S. High response methane sensor based on Au-modified hierarchical porous nanosheets-assembled ZnO microspheres. *Mater. Chem. Phys.* **2020**, *250*, No. 123027, DOI: 10.1016/j.matchemphys.2020.123027.

(11) Hu, J.; Gao, F.; Zhao, Z.; Sang, S.; Li, P.; Zhang, W.; Zhou, X.; Chen, Y. Synthesis and characterization of Cobalt-doped ZnO microstructures for methane gas sensing. *Appl. Surf. Sci.* **2016**, *363*, 181−188.

(12) Kooti, M.; Keshtkar, S.; Askarieh, M.; Rashidi, A. Progress toward a novel methane gas sensor based on SnO_2 nanorods-nanoporous graphene hybrid. *Sens. Actuators, B* **2019**, *281*, 96−106.

(13) Zhang, D.; Yin, N.; Xia, B. Facile fabrication of ZnO nanocrystalline-modified graphene hybrid nanocomposite toward methane gas sensing application. *J. Mater. Sci.:Mater. Electron.* **2015**, *26* (8), 5937−5945.

(14) Singh, A.; Sharma, A.; Tomar, M.; Gupta, V. Reduced graphene oxide-SnO_2 nanocomposite thin film based CNG/PNG sensor. *Sens. Actuators, B* **2017**, *245*, 590−598.

(15) Navazani, S.; Shokuhfar, A.; Hassanisadi, M.; Askarieh, M.; Di Carlo, A.; Agresti, A. Facile synthesis of a SnO_2@rGO nanohybrid

and optimization of its methane-sensing parameters. *Talanta* **2018**, *181*, 422−430.
(16) Zhang, S.; Li, Y.; Sun, G.; Zhang, B.; Wang, Y.; Cao, J.; Zhang, Z. Enhanced methane sensing properties of porous NiO nanaosheets by decorating with SnO_2. *Sens. Actuators, B* **2019**, *288*, 373−382.
(17) Shooshtari, M. Gold-decorated vertically aligned carbon nanofibers for high-performance room-temperature ethanol sensing. *Microchim. Acta* **2025**, *192*, 517.
(18) Monir, M. S. I.; Rahman, A.; Saha, P.; Rahman, I.; Mahiuddin, M. Towards greener reduced graphene oxide: a critical review of environmentally driven reduction strategies. *RSC Adv.* **2026**, *16* (3), 2044−2061.
(19) Lin, J.; Peng, Z.; Liu, Y.; Ruiz-Zepeda, F.; Ye, R.; Samuel, E. L.; Yacaman, M. J.; Yakobson, B. I.; Tour, J. M. Laser-induced porous graphene films from commercial polymers. *Nat. Commun.* **2014**, *5*, No. 5714.
(20) Chang, H.; Feng, S.; Qiu, X.; Meng, H.; Guo, G.; He, X.; He, Q.; Yang, X.; Ma, W.; Kan, R.; Fittschen, C.; Li, C. Implementation of the toroidal absorption cell with multi-layer patterns by a single ring surface. *Opt. Lett.* **2020**, *45* (21), 5897−5900.
(21) Ye, X.; Yang, Z.; Zheng, X.; Qiang, H.; Wei, M.; Li, Y.; Chen, M.; Luo, N. A review on the laser-induced synthesis of graphene and its applications in sensors. *J. Mater. Sci.* **2024**, *59* (26), 11644−11668.
(22) Moon, H.-r.; Ryu, B. Review of Laser-Induced Graphene (LIG) Produced on Eco-Friendly Substrates. *Int. J. Precis. Eng. Manuf.-Green Technol.* **2024**, *11* (4), 1279−1294.
(23) Chyan, Y.; Ye, R.; Li, Y.; Singh, S. P.; Arnusch, C. J.; Tour, J. M. Laser-Induced Graphene by Multiple Lasing: Toward Electronics on Cloth, Paper, and Food. *ACS Nano* **2018**, *12* (3), 2176−2183.
(24) Ding, H.; Wei, Y.; Wu, Z.; Tao, K.; Ding, M.; Xie, X.; Wu, J. Recent Advances in Gas and Humidity Sensors Based on 3D Structured and Porous Graphene and Its Derivatives. *ACS Mater. Lett.* **2020**, *2* (11), 1381−1411.
(25) Kim, Y.-J.; Le, T.-S. D.; Nam, H. K.; Yang, D.; Byunggi, K. Wood-based flexible graphene thermistor with an ultra-high sensitivity enabled by ultraviolet femtosecond laser pulses. *CIRP Ann.* **2021**, *70*, 443−446.
(26) Ye, R.; Chyan, Y.; Zhang, J.; Li, Y.; Han, X.; Kittrell, C.; Tour, J. M. Laser-Induced Graphene Formation on Wood. *Adv. Mater.* **2017**, *29* (37), No. 1702211, DOI: 10.1002/adma.201702211.
(27) Yang, L.; Ji, H.; Meng, C.; Li, Y.; Zheng, G.; Chen, X.; Niu, G.; Yan, J.; Xue, Y.; Guo, S.; Cheng, H. Intrinsically Breathable and Flexible NO_2 Gas Sensors Produced by Laser Direct Writing of Self-Assembled Block Copolymers. *ACS Appl. Mater. Interfaces* **2022**, *14* (15), 17818−17825.
(28) Santos-Ceballos, J. C.; Salehnia, F.; Romero, A.; Vilanova, X.Flexible Sensor Utilizing Polypyrrole Laser-Induced Graphene Nanocomposite for Room Temperature Ammonia Detection. In *2023 IEEE Sensors*; IEEE, 2023; pp 1−4.
(29) Dosi, M.; Lau, I.; Zhuang, Y.; Simakov, D. S. A.; Fowler, M. W.; Pope, M. A. Ultrasensitive Electrochemical Methane Sensors Based on Solid Polymer Electrolyte-Infused Laser-Induced Graphene. *ACS Appl. Mater. Interfaces* **2019**, *11* (6), 6166−6173.
(30) Yan, J.; Kang, Y.; Fang, W.; Zhu, B.; Song, Z. Tuning Gas Sensing Properties through Metal-Nanocluster Functionalization of 3D SnO_2 Nanotube Arrays for Selective Gas Detection. *ACS Sens.* **2025**, *10* (8), 6084−6094.
(31) Bai, H.; Feng, C.; Chen, Y.; Du, Y.; Feng, Y.; Liu, K.; Yan, Y.; Liu, J.; Zhang, B.; Wang, J.; Chen, D.; Zheng, Y.; Guo, F. Room temperature gas sensor based on porous NiO nanoplates modified with rGO nanosheets and SnO_2 nanoparticles for accurate and rapid ppb-level NO_2 detection. *Nano Mater. Sci.* **2026**, *8*, 36 DOI: 10.1016/j.nanoms.2024.12.006.
(32) Ju, X.; Feng, X.; Duan, X.; Cui, B.; Huang, G.; Chen, Y.; Tong, X.; Yang, Z.; Guo, P.; Xu, S.; Shi, J.-W. Interfacial engineering of MXene-induced nanoflower-like LDH heterostructures for enhanced CO_2 capture. *Sep. Purif. Technol.* **2026**, *385*, No. 136443.
(33) Shui, T.; Pan, M.; Lu, Y.; Zhang, J.; Liu, Q.; Nikrityuk, P. A.; Tang, T.; Liu, Q.; Zeng, H. High-efficiency and durable removal of water-in-heavy oil emulsions enabled by delignified and carboxylated basswood with zwitterionic nanohydrogel coatings. *J. Colloid Interface Sci.* **2022**, *612*, 445−458.
(34) Manikandan, V.; Petrila, I.; Vigneselvan, S.; Mane, R. S.; Vasile, B.; Dharmavarapu, R.; Lundgaard, S.; Juodkazis, S.; Chandrasekarang, J. A reliable chemiresistive sensor of nickel-doped tin oxide (Ni-SnO_2) for sensing carbon dioxide gas and humidity. *RSC Adv.* **2020**, *10*, 3796−3804.
(35) Kim, M.; Lee, S. M.; Jeon, J. W.; Movaghgharnezhad, S.; Jeong, H.; Moghaddam, F.; Mitchell, D.; Kang, P.; Kim, B. G. Photo-thermochemical Nanoassembly of 3D Porous Graphene and Palladium Nanoparticles for High-Performance Hydrogen Detection. *ACS Appl. Mater. Interfaces* **2021**, *13* (41), 49128−49136.
(36) Tesfahunegn, B. A.; Kleinberg, M. N.; Powell, C. D.; Arnusch, C. J. A Laser-Induced Graphene-Titanium(IV) Oxide Composite for Adsorption Enhanced Photodegradation of Methyl Orange. *Nanomaterials* **2023**, *13* (5), No. 947, DOI: 10.3390/nano13050947.
(37) Zhang, J.; Zeng, D.; Zhu, Q.; Wu, J.; Huang, Q.; Zhang, W.; Xie, C. Enhanced room temperature NO_2 response of NiO-SnO_2 nanocomposites induced by interface bonds at the p-n heterojunction. *Phys. Chem. Chem. Phys.* **2016**, *18* (7), 5386−5396.
(38) Khandelwal, M.; Nguyen, A. P.; Tran, C. V.; In, J. B. Simple fabrication of Co_3O_4 nanoparticles on N-doped laser-induced graphene for high-performance supercapacitors. *RSC Adv.* **2021**, *11* (61), 38547−38554.
(39) Sun, X.; Li, M.; Wang, Y.; Qin, C.; Cao, J.; Wang, Y. NiO/ZnO heterojunction microspheres for methane detection at room temperature. *Opt. Mater.* **2024**, *148*, No. 114893, DOI: 10.1016/j.optmat.2024.114893.
(40) Li, J.; Yu, X.; Sun, R.; Li, H.; Zhu, X.; Ma, Y.; Ma, L. One-step synthesis of Co_3O_4 nanoparticles/laser induced graphene composites in ambient condition for electrocatalytic OER reaction. *Carbon Trends* **2023**, *12*, No. 100285, DOI: 10.1016/j.cartre.2023.100285.
(41) Yang, L.; Zheng, G.; Cao, Y.; Meng, C.; Li, Y.; Ji, H.; Chen, X.; Niu, G.; Yan, J.; Xue, Y.; Cheng, H. Moisture-resistant, stretchable NO(x) gas sensors based on laser-induced graphene for environmental monitoring and breath analysis. *Microsyst. Nanoeng.* **2022**, *8*, No. 78.
(42) Soydan, G.; Ergenc, A. F.; Alpas, A. T.; Solak, N. Development of an $NO_{(2)}$ Gas Sensor Based on Laser-Induced Graphene Operating at Room Temperature. *Sensors* **2024**, *24* (10), No. 3217, DOI: 10.3390/s24103217.
(43) Bressi, A. C.; Dallinger, A.; Steksova, Y.; Greco, F. Bioderived Laser-Induced Graphene for Sensors and Supercapacitors. *ACS Appl. Mater. Interfaces* **2023**, *15* (30), 35788−35814.
(44) Martins, L.; Kulyk, B.; Theodosiou, A.; Ioannou, A.; Moreirinha, C.; Kalli, K.; Santos, N.; Costa, F.; Pereira, S. O.; Marques, C. Laser-induced graphene from commercial polyimide coated optical fibers for sensor development. *Opt. Laser Technol.* **2023**, *160*, No. 109047, DOI: 10.1016/j.optlastec.2022.109047.
(45) Yogi, S.; Kumar, P.; Zulfequar, M.; Jain, V. K.; Kumar, A. High performance methane gas sensor based on the heterojunction of RGO/TiO_2 on SiNWs. *J. Mater. Sci.:Mater. Electron.* **2025**, *36* (24), No. 1526, DOI: 10.1007/s10854-025-15621-1.
(46) Shaalan, N. M.; Rashad, M.; Moharram, A. H.; Abdel-Rahim, M. A. Promising methane gas sensor synthesized by microwave-assisted Co_3O_4 nanoparticles. *Mater. Sci. Semicond. Process.* **2016**, *46*, 1−5.
(47) Wang, Y.; Zhang, H.; Cao, J. Synthesis and low temperature methane sensing performance of Pd modified In_2O_3 microspheres. *Mater. Chem. Phys.* **2022**, *279*, No. 125749, DOI: 10.1016/j.matchemphys.2022.125749.
(48) Li, L.; Zhang, J.; Song, Y.; Dan, R.; Xia, X.; Zhao, J.; Xu, R. Flexible Humidity Sensor Based on a Graphene Oxide Carbon Nanotube-Modified Co_3O_4 Nanoparticle-Embedded Laser-Induced Graphene Electrode. *ACS Appl. Mater. Interfaces* **2024**, *16* (26), 33981−33992.
(49) Nasresfahani, S.; Sheikhi, M. H.; Tohidi, M.; Zarifkar, A. Methane gas sensing properties of Pd-doped SnO_2 /reduced graphene

oxide synthesized by a facile hydrothermal route. *Mater. Res. Bull.* **2017**, *89*, 161−169.
(50) Das, A.; Bonu, V.; Prasad, A. K.; Panda, D.; Dhara, S.; Tyagi, A. K. The role of SnO_2 quantum dots in improved CH_4 sensing at low temperature. *J. Mater. Chem. C* **2014**, *2* (1), 164−171.
(51) Navazani, S.; Shokuhfar, A.; Hassanisadi, M.; Di Carlo, A.; Shahcheraghi, N. Fabrication and characterization of a sensitive, room temperature methane sensor based on SnO_2@reduced graphene oxide-polyaniline ternary nanohybrid. *Mater. Sci. Semicond. Process.* **2018**, *88*, 139−147.
(52) Zhang, D.; Chang, H.; Li, P.; Liu, R. Characterization of nickel oxide decorated-reduced graphene oxide nanocomposite and its sensing properties toward methane gas detection. *J. Mater. Sci.:Mater. Electron.* **2016**, *27* (4), 3723−3730.
(53) Alipour Baladeh, S.; Haratizadeh, H. High-performance methane gas sensor with low detection limit based on hydrothermally synthesized VO_2 nanostructure. *J. Mater. Sci.:Mater. Electron.* **2025**, *36* (20), No. 1277.
(54) Farahmandpour, M.; Sadeghfar, F.; Asfaram, A.; Ghaedi, M.; Javadian, H. Improving the sensitivity and detection speed of methane gas at room temperature using a nanosensor based on lead sulfide (PbS) colloidal quantum dots. *Results Chem.* **2025**, *18*, No. 102760.

https://doi.org/10.1021/acsomega.5c13608
ACS Omega 2026, 11, 24334−24345